

# Incommensurate broken-helix and broken-fanlike states in axion insulator candidate $\text{EuIn}_2\text{As}_2$

Masaki Gen,<sup>1,\*</sup> Yukako Fujishiro,<sup>1</sup> Kazuki Okigami,<sup>2</sup> Satoru Hayami,<sup>3</sup> Kiyohiro Adachi,<sup>4</sup> Daisuke Hashizume,<sup>4</sup> Takashi Kurumaji,<sup>5,6</sup> Hajime Sagayama,<sup>7</sup> Hironori Nakao,<sup>7</sup> Yoshinori Tokura,<sup>1,2,8</sup> and Taka-hisa Arima<sup>1,5</sup>

<sup>1</sup>RIKEN Center for Emergent Matter Science (CEMS), Wako 351-0198, Japan

<sup>2</sup>Department of Applied Physics, University of Tokyo, Tokyo 113-8656, Japan

<sup>3</sup>Graduate School of Science, Hokkaido University, Sapporo 060-0810, Japan

<sup>4</sup>Materials Characterization Support Team, RIKEN Center for Emergent Matter Science (CEMS), Wako 351-0198, Japan

<sup>5</sup>Department of Advanced Materials Science, University of Tokyo, Kashiwa 277-8561, Japan

<sup>6</sup>Division of Physics, Mathematics and Astronomy, California Institute of Technology, Pasadena, California 91125, USA

<sup>7</sup>Institute of Materials Structure Science, High Energy Accelerator Research Organization, Tsukuba 305-0801, Japan

<sup>8</sup>Tokyo College, University of Tokyo, Tokyo 113-8656, Japan

(Dated: March 6, 2024)

Zintl phase  $\text{EuIn}_2\text{As}_2$  has garnered growing attention as an axion insulator candidate, triggered by the identification of a commensurate double- $\mathbf{Q}$  broken-helix state in previous studies, however, its periodicity and symmetry remain subjects of debate. Here, we perform resonant x-ray scattering experiments on  $\text{EuIn}_2\text{As}_2$ , revealing an incommensurate nature of the broken-helix state, where both the wave number and the amplitude of the helical modulation exhibit systematic sample dependence. Furthermore, the application of an in-plane magnetic field brings about a broken-fanlike state preserving the double- $\mathbf{Q}$  nature, which could be attributed to multiple-spin interactions in momentum space. We propose that the itinerant character of  $\text{EuIn}_2\text{As}_2$ , possibly induced by Eu deficiency, gives rise to the helical modulation and impedes the realization of a theoretically-predicted axion state with the collinear antiferromagnetic order.

Europium-based compounds offer a fertile playground for exploring nontrivial magnetotransport phenomena [1–4]. In the presence of Fermi surfaces, the carrier-mediated Ruderman-Kittel-Kasuya-Yosida (RKKY) interaction can stabilize a variety of modulated magnetic structures such as helix [5–8] and skyrmions [9–13]. The correlation between magnetism and electronic band topology is one other intriguing aspect, as extensively studied in the 122 families of the Zintl phase [14–20]. First-principles calculations predict that  $\text{EuIn}_2\text{As}_2$  can host an axion insulating state (AXS) with the layered antiferromagnetic (AFM) order [21, 22], thereby potentially exhibiting the quantized magnetoelectric effect [23–25]. Given that the AXS remains unestablished in stoichiometric bulk materials [25–30], a comprehensive investigation on the physical properties of  $\text{EuIn}_2\text{As}_2$  stands as a critical issue [31–41], not only from the fundamental viewpoint but also for its applications in next-generation devices [23].

$\text{EuIn}_2\text{As}_2$  forms a hexagonal crystal structure of space group  $P6_3/mmc$ , consisting of alternating stacking of Eu triangular layers and  $\text{In}_2\text{As}_2$  blocks [Fig. 1(a)] (Note that one unit cell contains two Eu layers). The magnetism is dominated by intraplane ferromagnetic and interplane AFM interactions between localized  $\text{Eu}^{2+}$  moments, with an easy-plane anisotropy becoming evident at low temperatures [32]. Despite the theoretical prediction of a gapped insulating state [22], angle-resolved photoemission spectroscopies (ARPES) revealed holelike bulk bands crossing the Fermi level [33, 34]. Neutron diffraction (ND) [39] and resonant x-ray scattering (RXS) experiments [40] observed a concurrent short-period magnetic modulation,  $\mathbf{Q}_1 = (0, 0, q_{1z})$ , along with the AFM component  $\mathbf{Q}_2 = (0, 0, 1)$ ; the reported  $q_{1z}$  values are 0.303(1) [39] and 0.3328(6) [40], respectively, in the reciprocal-lattice unit. A phase separation scenario was excluded by azimuthal

scans in the RXS [40]. Both studies proposed a six-layer-period double- $\mathbf{Q}$  helical structure, termed *broken helix*, under the assumption that  $\mathbf{Q}_1$  represents an exactly commensurate modulation with  $q_{1z} = 1/3$  [39, 40]. Initially, the AXS was believed to be realized in the commensurate broken-helix state, as the  $\mathcal{TC}_2$  symmetry (the combination of time-reversal and two-fold rotational operations) is preserved once the principal axis of the broken helix is aligned along a specific crystallographic axis [39, 40]. However, a recent optical birefringence study challenged the above picture in terms of the symmetry, and proposed the unpinned nature of the broken helix owing to minimal hexagonal anisotropy [41].

Here, we reexamine the magnetic structure of  $\text{EuIn}_2\text{As}_2$ . While the preceding ND study identified an *incommensurate*  $\mathbf{Q}_1$  modulation [39], no incommensurate spin configuration has been considered so far [39–41]. Whether  $\mathbf{Q}_1$  is commensurate or not is pivotal, as the latter is not compatible with the AXS due to the  $\mathcal{TC}_2$  symmetry breaking. The mechanism for the emergence of the  $\mathbf{Q}_1$  modulation also remains puzzling [40, 41]. To address these issues, we perform the RXS experiments, revealing that the  $\mathbf{Q}_1$  peak exhibits variability in the  $q_{1z}$  value (0.25–0.29) as well as the intensity across samples [Fig. 1(b)]. The complementary single-crystal structure analysis suggests that the  $\mathbf{Q}_1$  modulation stems from the RKKY interaction mediated by doped holes due to Eu deficiency. We argue that, to avoid the loss of generality, the broken-helix state should be considered as a superposition of incommensurate helical and collinear AFM modulations, as illustrated in Fig. 1(c). We also reveal the appearance of a double- $\mathbf{Q}$  fanlike state with higher-harmonic modulations in an in-plane magnetic field, giving insights into a theoretical framework to describe the complicated magnetism in  $\text{EuIn}_2\text{As}_2$ .

Single crystals of  $\text{EuIn}_2\text{As}_2$  were grown by an indium flux

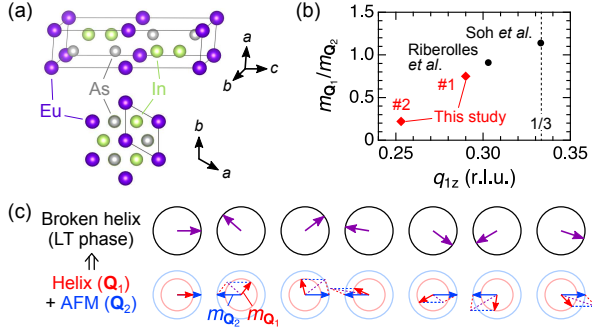


FIG. 1. (a) Crystal structure of  $\text{EuIn}_2\text{As}_2$ . The black line represents a crystallographic unit cell. (b) Ratio of the magnetic-moment amplitude of the  $\mathbf{Q}_1 = (0, 0, q_{1z})$  and  $\mathbf{Q}_2 = (0, 0, 1)$  modulations,  $m_{\mathbf{Q}_1}/m_{\mathbf{Q}_2}$ , versus the  $q_{1z}$  value in the broken-helix state for samples used in this study (5 K) and those in previous studies by Riberrolles *et al.* [39] and by Soh *et al.* [40] (6 K).  $m_{\mathbf{Q}_1}/m_{\mathbf{Q}_2}$  is estimated from the observed peak intensities. (c) Schematics of the broken-helix state and an equivalent double- $\mathbf{Q}$  representation as the superposition of incommensurate helical  $\mathbf{Q}_1$  and collinear AFM  $\mathbf{Q}_2$  modulations. Magnetic moments are in the  $ab$ -plane, and the modulation is along the  $c$  axis.

method. Details of sample growth and characterization are described in the Supplemental Material (SM) [42]. We picked up two specimens (#1 and #2) from the same batch for the RXS. RXS experiments were performed at BL-3A, Photon Factory, KEK, by using horizontally ( $\pi$ ) polarized incident x-rays in resonance with the Eu  $L_2$  absorption edge ( $E = 7.612$  keV) [7, 11]. Samples with the as-grown (001) plane were glued on an aluminium plate and set in a cryostat equipped with a vertical-field superconducting magnet. The scattering plane was set to be  $(H, 0, L)$ , and a magnetic field was applied along the crystallographic  $b$  axis [Fig. 2(a)]. We could access fundamental Bragg peaks at  $(3m, 0, 2n)$  and  $(3m \pm 1, 0, n)$  ( $m, n$ : integer), and their magnetic satellite peaks in the reciprocal space [Fig. 2(b)]. Unless otherwise stated, we performed the  $(0, 0, L)$  scan with  $L = 12$ –16, and the scattered x-rays were detected without analyzing the  $\pi'$  and  $\sigma'$  polarizations, parallel and perpendicular to the scattering plane, respectively. For polarization analysis, the 006 reflection of a pyrolytic graphite (PG) crystal was used, where the scattering angle was  $\sim 92^\circ$  near the Eu  $L_2$  edge.

As in Refs. [39, 40], we observe two kinds of magnetic Bragg peaks,  $\mathbf{Q}_1 = (0, 0, q_{1z})$  and  $\mathbf{Q}_2 = (0, 0, 1)$  [Fig. 2(c)]. Figures 2(d)–2(f) show the temperature dependence of magnetic susceptibility,  $q_{1z}$ , and integrated intensities of the  $\mathbf{Q}_1$  and  $\mathbf{Q}_2$  peaks in (nearly) zero field for sample #1. Upon cooling, the  $\mathbf{Q}_1$  and  $\mathbf{Q}_2$  peaks emerge below  $T_{N1} = 17.6$  K and  $T_{N2} = 16.2$  K, respectively.  $q_{1z}$  gradually decreases from 0.32 to 0.29 in the intermediate-temperature (IT) phase, while  $q_{1z}$  is almost temperature independent in the low-temperature (LT) phase. These trends also agree with Refs. [39, 40], although there is a discrepancy in the  $q_{1z}$  value [Fig. 1(b)]. Notably, a distinct  $q_{1z}$  value of 0.25 is observed for sample #2, and we confirm that the way of adhering samples to the Al plate has little influence on  $q_{1z}$  (see the SM [42]). Therefore, the observed variability in  $q_{1z}$  appears to be primarily attributed to

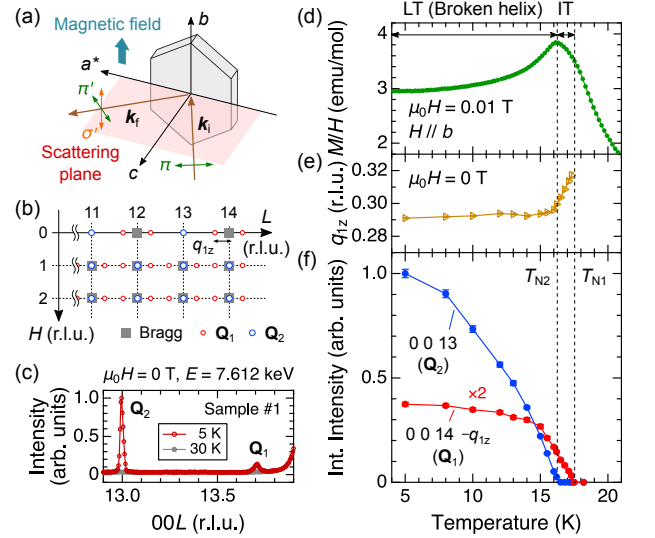


FIG. 2. (a) Experimental geometry of the RXS.  $\mathbf{k}_i$  ( $\mathbf{k}_f$ ) and  $\pi$  ( $\pi'$  and  $\sigma'$ ) represent the propagation vector and polarization direction of incident (scattered) x-rays, respectively. (b) Positions of the Bragg peaks in the  $(H, 0, L)$  scattering plane below  $T_{N2}$ . Gray squares are the fundamental peaks, and red (blue) circles are the magnetic  $\mathbf{Q}_1$  ( $\mathbf{Q}_2$ ) peaks. (c) RXS profiles observed in the  $(0, 0, L)$  scan at 5 K (red) and 30 K (gray) in zero field for sample #1. [(d)–(f)] Temperature dependence of (d) magnetic susceptibility  $M/H$ , (e)  $q_{1z}$ , and (f) integrated intensity of the 00L reflections with  $L = 14 - q_{1z}$  and  $L = 13$  in zero field.

the sample dependence rather than extrinsic strain.

Indeed, our single-crystal structural analyses reveal a Eu deficiency of 1.6(5)% for sample #1 and 1.1(4)% for sample #2 (see the SM [42]), indicating that a larger Eu deficiency leads to a larger  $q_{1z}$  value. Recalling the first-principles calculations predicting a gapped insulating state with the AFM order ( $\mathbf{Q}_2$ ) [22], the additional  $\mathbf{Q}_1$  modulation is expected to be induced by doped hole carriers which contribute to the RKKY interaction between the  $\text{Eu}^{2+}$  moments. We also find that the intensity ratio of the  $\mathbf{Q}_1$  to the  $\mathbf{Q}_2$  peak is higher for samples with larger  $q_{1z}$  [Fig. 1(b)], suggesting that the  $\mathbf{Q}_1$  component is enhanced by a larger number of carriers. The above scenarios agree with the 3D character of a hole pocket observed in a previous ARPES [33], although the details of the Fermi-surface shape need to be clarified to comprehend the quantitative correlation between the carrier number (related to the off-stoichiometry) and the magnetic modulation period.

Next, we investigate the magnetic structure changes with the application of an in-plane magnetic field for sample #1, which undergoes a metamagnetic transition at  $\mu_0 H_{c1} = 0.2$  T at 5 K [32, 35, 40]. Figures 3(a)–(c) show the field dependence of magnetization,  $q_{1z}$ , and integrated intensities of the  $\mathbf{Q}_1$  and  $\mathbf{Q}_2$  peaks. With increasing a magnetic field, both  $\mathbf{Q}_1$  and  $\mathbf{Q}_2$  peaks survive until the saturation field of 1.0 T. Here,  $q_{1z}$  exhibits only a small change of at most  $\pm 0.01$  even across  $H_{c1}$ . With subsequently decreasing a magnetic field, a hysteresis appears around  $H_{c1}$  in RXS, in line with the magnetization process. Ultimately, neither the intensities of the  $\mathbf{Q}_1$  and  $\mathbf{Q}_2$

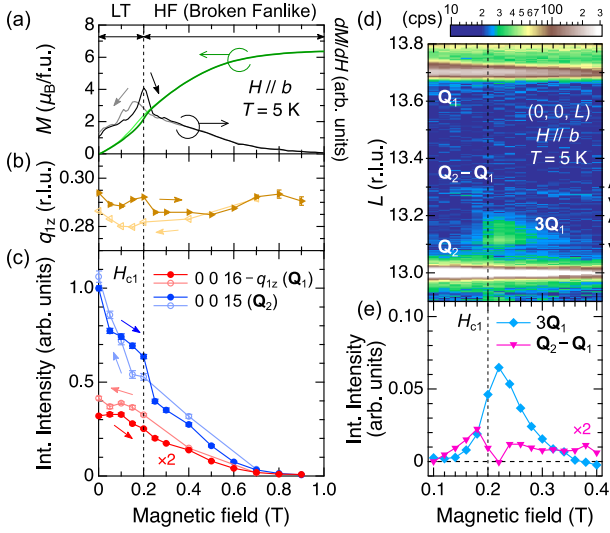


FIG. 3. [(a)–(c)] Magnetic-field dependence of (a) magnetization  $M$  (left axis) and its field derivative  $dM/dH$  (right axis), (b)  $q_{1z}$ , and (c) integrated intensity  $I(H)$  of the  $00L$  reflections with  $L = 16 - q_{1z}$  and  $L = 15$ . Dark and light colors represent data in field-increasing and decreasing processes, respectively. (d) Logarithmic contour plot of the RXS intensity in the  $(0, 0, L)$  scan near  $H_{c1}$  in a field-increasing process. Black arrows on the right represent peak widths for  $3Q_1$  and  $Q_2 - Q_1$ . (e) Magnetic-field dependence of the integrated intensity of the  $3Q_1$  (cyan) and  $Q_2 - Q_1$  (pink) peaks. The absolute value is normalized by the intensity of the  $0013$  reflection at 0 T. All the data are taken at 5 K with  $H \parallel b$ .

peaks nor  $q_{1z}$  reverts to the original values at zero field.

We find remarkable features in the RXS profiles near  $H_{c1}$ . Figure 3(d) shows a logarithmic contour plot of the RXS intensity against a magnetic field, observed in the  $(0, 0, L)$  scan in the  $L$  range between 12.9 and 13.8. Apart from the strong  $Q_1$  and  $Q_2$  peaks at  $L = 13.71$  and 13, respectively, peaks around  $L = 13.29$  and 13.13 are discernible in certain field ranges. These additional peaks likely correspond to higher-harmonic  $Q_2 - Q_1$  and  $3Q_1$  modulations, respectively. The field evolution of integrated intensities of these peaks are displayed in Fig. 3(e). The weak  $Q_2 - Q_1$  peak appears above 0.1 T and persists until at least 0.4 T, except immediately after  $H_{c1}$  where the intensity of the  $3Q_1$  peak becomes prominent. Notably, a  $2Q_1$  peak at  $L = 13.42$ , expected in the conventional fanlike structure [46, 47], is not observed in the entire field range [Fig. 3(d)]. These results indicate that the high-field (HF) phase above  $H_{c1}$  is characterized by a superposition of  $Q_1$  and  $Q_2$ , ruling out a phase separation scenario.

To get information on the orientation of magnetic moments in each phase at 5 K, we performed polarization analysis with  $H \parallel b$ . In general, the magnetic scattering intensity  $I$  is given by  $I \propto (\mathbf{e}_i \times \mathbf{e}_f) \cdot \mathbf{m}_Q$ , where  $\mathbf{e}_i$  ( $\mathbf{e}_f$ ) is the polarization vector of the incident (scattered) beam, and  $\mathbf{m}_Q$  is a magnetic moment of the  $Q$  modulation. The  $\pi-\pi'$  channel ( $I_{\pi-\pi'}$ ) always detects the modulated component along  $b$  ( $m_b$ ), whereas the  $\pi-\sigma'$  channel ( $I_{\pi-\sigma'}$ ) contains those along  $a^*$  ( $m_a$ ) and  $c$  ( $m_c$ ) in the ratio of  $\cos^2 \omega : \sin^2 \omega$ , where  $\omega$  is the angle between the propagation vector of the incident beam ( $\mathbf{k}_i$ ) and the  $a^*$

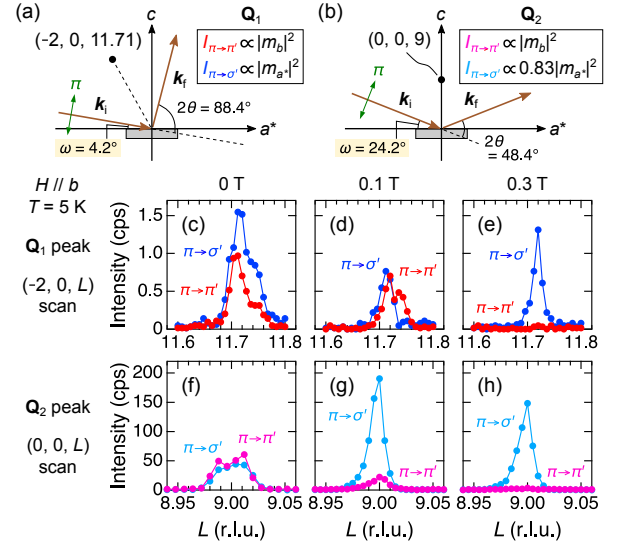


FIG. 4. [(a)(b)] Schematic geometrical configuration of the RXS focusing on the  $Q_1$  and  $Q_2$  peaks around the magnetic Bragg spots  $(-2, 0, 11.71)$  and  $(0, 0, 9)$ , respectively. See also Figs. 2(a) and (b). [(c)–(h)] RXS profiles of the polarization analysis at 5 K at 0 T [(c)(f)], 0.1 T [(d)(g)], and 0.3 T [(e)(h)] with  $H \parallel b$ . Panels (c)–(e) and (f)–(h) show the data of the  $(-2, 0, L)$  scan around  $L = 11.71$  and  $(0, 0, L)$  scan around  $L = 9$ , respectively.

axis. Figures 4(a) and 4(b) show the experimental configurations of polarization analysis focusing on the Bragg spots at  $(-2, 0, 11.71)$  and  $(0, 0, 9)$ , in which  $I_{\pi-\sigma'}$  mainly reflects  $m_a$  ( $\sim 100\%$  and  $83\%$ ) of the  $Q_1$  and  $Q_2$  modulations, respectively. Additional measurements focusing on the Bragg spots at  $(2, 0, 11.71)$  and  $(0, 0, 17)$  confirm the absence of  $m_c$  (see the SM [42]), i.e., all the spins lie within the  $ab$  plane.

At zero field, both  $I_{\pi-\pi'}$  and  $I_{\pi-\sigma'}$  have intensities at  $(-2, 0, 11.71)$  and  $(0, 0, 9)$  [Figs. 4(c) and 4(f)]. At 0.1 T ( $< H_{c1}$ ), a drastic enhancement is observed in  $I_{\pi-\sigma'}$  at  $(0, 0, 9)$ , accompanied by a suppression of  $I_{\pi-\pi'}$  [Fig. 4(g)], suggesting the reorientation of magnetic domains so as to lie the AFM component perpendicular to the field direction. In contrast,  $I_{\pi-\pi'}$  and  $I_{\pi-\sigma'}$  still have comparable intensities at  $(-2, 0, 11.71)$  [Fig. 4(d)], suggesting that the  $Q_1$  modulation originates from a helical component, rather than sinusoidal. Followed by the metamagnetic transition, the presence of only  $m_a$  is confirmed for both the  $Q_1$  and  $Q_2$  modulations, as evidenced by the disappearance of  $I_{\pi-\pi'}$  at the both Bragg positions at 0.3 T ( $> H_{c1}$ ) [Figs. 4(e) and 4(h)]. Accordingly, the HF phase can be ascribed to a double- $Q$  fanlike state.

Let us here update the understanding of the magnetic structure in  $\text{EuIn}_2\text{As}_2$ . We show that the LT phase is a broken-helix state with a superposition of incommensurate helical  $Q_1$  and AFM  $Q_2$  modulations, which can be approximately described as  $\mathbf{m}(\mathbf{r}) \propto (1, i, 0) \sum_{\eta=1,2} m_{Q_\eta} \exp(i\mathbf{Q}_\eta \cdot \mathbf{r}) + \text{c.c.}$  in zero field. This expression encompasses the commensurate broken helix proposed in Refs. [39, 40] as a special case. By comparing the observed intensities of the  $Q_1$  and  $Q_2$  peaks with the calculated ones based on the above formula assuming an equal moment-size condition, we estimate  $m_{Q_1}/m_{Q_2}$  at

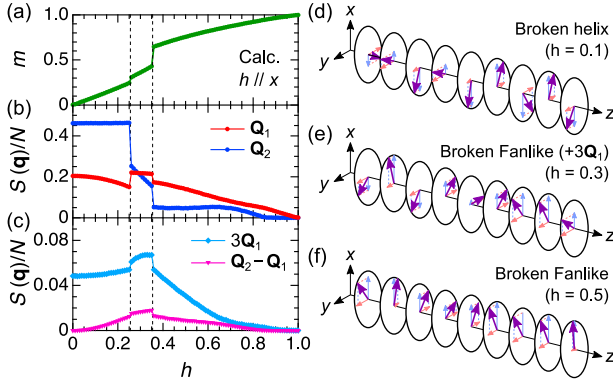


FIG. 5. Magnetic-field dependence of (a) magnetization  $m$ , and (b)(c) spin structure factor  $S(\mathbf{q})$  per a spin at several  $\mathbf{Q}$ 's for  $h \parallel x$ , calculated by simulated annealing for Eq. (1) with  $K = 0.9$ ,  $\alpha = 0.48$ , and  $\alpha' = 0.9$ . Local spin configurations at  $h = 0.1, 0.3$ , and  $0.5$  are schematically illustrated by purple arrows in panels (d), (e), and (f), respectively. The light blue (red) arrow indicates the  $x$  ( $y$ ) component of each spin.

the lowest temperature for each sample used in this study and in Refs. [39, 40], as shown in Fig. 1(b) (see the SM [42]); e.g.,  $m_{\mathbf{Q}_1}/m_{\mathbf{Q}_2} \approx 0.75$  and  $0.22$  for samples #1 ( $q_{1z} = 0.29$ ) and #2 ( $q_{1z} = 0.25$ ), respectively. A positive correlation between  $q_{1z}$  and  $m_{\mathbf{Q}_1}/m_{\mathbf{Q}_2}$  can be clearly seen, which agrees with the RKKY picture for the emergence of helimagnetism by hole doping, as mentioned above. We also note that the IT phase was identified as a sinusoidal state by Mössbauer [39] and optical birefringence measurements [41]. As the hexagonal anisotropy is negligibly weak [32, 41], it is natural to believe that the sinusoidal modulation is stabilized by thermal fluctuations and gradually transforms into helix with decreasing temperature. We thus infer that there is a slight elliptical distortion of the  $\mathbf{Q}_1$  component in the LT phase at 5 K.

Our RXS also reveals a helix-fan transition while keeping the double- $\mathbf{Q}$  nature, as evidenced by the observation of higher harmonics  $\mathbf{Q}_2 - \mathbf{Q}_1$ . Since the real-space picture of the double- $\mathbf{Q}$  fanlike state is rather nontrivial, a theoretical description based on the microscopic model is necessary. We first investigate ground states of a spin Hamiltonian composed of long-range Heisenberg exchange and biquadratic exchange interactions in real space on a 1D chain system, as proposed in Ref. [41]. Our variational calculations reveal that this model can stabilize an incommensurate broken helix with a dominant  $\mathbf{Q}_2$  component in zero field, while it fails to preserve the double- $\mathbf{Q}$  nature and instead stabilizes a canted AFM state in high magnetic fields (see the SM [42]).

In order to reproduce the double- $\mathbf{Q}$  fanlike state in the HF phase, we employ an effective spin Hamiltonian composed of exchange interactions in momentum space:

$$\begin{aligned} \mathcal{H} = & -JS_{\mathbf{Q}_1} \cdot \mathbf{S}_{-\mathbf{Q}_1} - J'S_{\mathbf{Q}_2} \cdot \mathbf{S}_{-\mathbf{Q}_2} - J''S_{\mathbf{Q}_3} \cdot \mathbf{S}_{-\mathbf{Q}_3} \\ & + K(S_{\mathbf{Q}_1} \cdot \mathbf{S}_{-\mathbf{Q}_1})^2 + K'(S_{\mathbf{Q}_2} \cdot \mathbf{S}_{-\mathbf{Q}_2})^2 + K''(S_{\mathbf{Q}_3} \cdot \mathbf{S}_{-\mathbf{Q}_3})^2 \\ & - K_2(S_{\mathbf{Q}_1} \cdot \mathbf{S}_{\mathbf{Q}_2})(\mathbf{S}_{-\mathbf{Q}_1} \cdot \mathbf{S}_{-\mathbf{Q}_2}) - h \sum_i S_i^x, \end{aligned} \quad (1)$$

where we take into account dominant interactions with  $\mathbf{Q}_1 =$

$0.29\pi$  and  $\mathbf{Q}_2 = \pi$ . In addition to the conventional bilinear and biquadratic terms for  $\mathbf{Q}_1$  and  $\mathbf{Q}_2$  [49], Eq. (1) includes an intertwined coupling term ( $K_2$ ) with a negative sign, which plays a crucial role in stabilizing a double- $\mathbf{Q}$  fanlike state in high magnetic fields. We also introduce higher-harmonic terms ( $J''$  and  $K''$ ) with  $\mathbf{Q}_3 = 3\mathbf{Q}_1$  to reproduce the enhancement of the  $3\mathbf{Q}_1$  modulation immediately after the metamagnetic transition. The last term in Eq. (1) represents the Zeeman coupling to an in-plane magnetic field  $h \parallel x$ . For simplicity, we set  $J' = \alpha J$ ,  $J'' = \alpha' J$ ,  $K' = \alpha^2 K$ ,  $K'' = \alpha'^2 K$ ,  $K_2 = K/2$ ,  $J = 1$  as the energy unit, and consider XY spins with  $|\mathbf{S}_i| = 1$ . We performed simulated annealing with  $N = 200$  spins for several parameter sets, and calculated the magnetization  $m$  and spin structure factor, defined as  $S(\mathbf{q}) = (1/N) \sum_{i,j} \langle \mathbf{S}_i \cdot \mathbf{S}_j \rangle e^{i\mathbf{q} \cdot (\mathbf{r}_i - \mathbf{r}_j)}$ . Figures 5(a)–5(c) show one typical result, which qualitatively reproduces our RXS data (Fig. 3). The system undergoes metamagnetic transitions, accompanied by the enhancement of  $S(3\mathbf{Q}_1)$  and  $S(\mathbf{Q}_2 - \mathbf{Q}_1)$ . We note that other parameter sets can bring about qualitatively distinct behaviors in higher harmonics, such as the enhancement of  $S(\mathbf{Q}_2 - 2\mathbf{Q}_1)$  instead of  $S(3\mathbf{Q}_1)$ .

Figures 5(d)–5(f) show schematics of local spin configurations in three different phases at  $h = 0.1, 0.3$ , and  $0.5$ , respectively. The spin configuration at  $h = 0.3$  is far from the conventional fanlike state in that some spins still possess a negative  $x$  component. Notably, a square-wave-shaped modulation appears in the  $y$  component (perpendicular to  $h$ ), reflecting the effect of  $3\mathbf{Q}_1$  along with the  $\mathbf{Q}_1$  modulation. At  $h = 0.5$ , the spin configuration is like a conventional fanlike state, while the remaining  $\mathbf{Q}_2$  component contributes to a complex manner of the spin flipping, resulting in a broken fanlike state. Though our magnetization data [Fig. 3(a)] shows no clear signs of a transition between these field-induced phases, the above-mentioned pictures would qualitatively describe the field evolution of a magnetic structure above  $H_{c1}$  in  $\text{EuIn}_2\text{As}_2$ . There have been reports of other Eu-based itinerant magnets exhibiting the coexistence of two magnetic modulations along the  $c$  axis, such as  $\text{EuRh}_2\text{As}_2$  [5],  $\text{EuCuSb}$  [6], and  $\text{EuZnGe}$  [7], although their in-field magnetic structures have yet to be understood. The present study establishes benchmark experimental and theoretical approaches for a better understanding of the complex helimagnetism characterized by interplane magnetic modulations.

In summary, we elucidate the incommensurate nature of the broken-helix state in  $\text{EuIn}_2\text{As}_2$  through RXS experiments, contradicting the previously proposed commensurate broken-helix [39, 40]. Furthermore, we identify the emergence of a broken fanlike state with higher-harmonic modulations in an in-plane magnetic field. The double- $\mathbf{Q}$  nature likely arises from the RKKY mechanism via hole carriers introduced by Eu deficiency. We propose that electron doping in *off-stoichiometric*  $\text{EuIn}_2\text{As}_2$  through chemical substitution can be a promising pathway to shift the Fermi energy to the band gap and suppress the helical modulation, realizing the theoretically predicted AXS with the collinear AFM order [22].

This work was financially supported by the JSPS KAK-

ENHI Grants-In-Aid for Scientific Research (No. 22H00101, No. 22K14011, No. 23H04869, No. 23H05431, and No. 23K13068), JST SPRING (No. JPMJSP2108), and JST PRESTO (No. MJPR20L8). The resonant x-ray scattering experiments were performed with the approval of the Photon Factory Program Advisory Committee (Proposal No. 2022G551 and No. 2023G093). The authors appreciate A. Kikkawa and M. Kriener for the invaluable support in the synthesis of the single crystals used in this study. The authors appreciate H. Takeda, S. Kitou, M. Hirschberger, and K. Kakurai for fruitful discussions.

---

\* [masaki.gen@riken.jp](mailto:masaki.gen@riken.jp)

- [1] G. A. Wigger, C. Beeli, E. Felder, H. R. Ott, A. D. Bianchi, and Z. Fisk, Percolation and the Colossal Magnetoresistance of Eu-Based Hexaboride, *Phys. Rev. Lett.* **93**, 147203 (2004).
- [2] K. Kawashima, T. Kinjo, T. Nishio, S. Ishida, H. Fujihisa, Y. Gotoh, K. Kihou, H. Eisaki, Y. Yoshida, and A. Iyo, Superconductivity in Fe-Based Compound  $\text{EuAFe}_4\text{As}_4$  (A = Rb and Cs), *J. Phys. Soc. Jpn.* **85**, 064710 (2016).
- [3] P. Rosa, Y. Xu, M. Rahn, J. Souza, S. Kushwaha, L. Veiga, A. Bombardi, S. Thomas, M. Janoschek, E. Bauer, M. Chan, Z. Wang, J. Thompson, N. Harrison, P. Pagliuso, A. Bernevig, and F. Ronning, Colossal magnetoresistance in a nonsymmorphic antiferromagnetic insulator, *npj Quantum Mater.* **5**, 52 (2020).
- [4] A. H. Mayo, H. Takahashi, M. S. Bahramy, A. Nomoto, H. Sakai, and S. Ishiwata, Magnetic Generation and Switching of Topological Quantum Phases in a Trivial Semimetal  $\alpha\text{-EuP}_3$ , *Phys. Rev. X* **12**, 011033 (2023).
- [5] S. Nandi, A. Kreyssig, Y. Lee, Y. Singh, J. W. Kim, D. C. Johnston, B. N. Harmon, and A. I. Goldman, Magnetic ordering in  $\text{EuRh}_2\text{As}_2$  studied by x-ray resonant magnetic scattering, *Phys. Rev. B* **79**, 100407(R) (2009).
- [6] H. Takahashi, K. Aono, Y. Nambu, R. Kiyonagi, T. Nomoto, M. Sakano, K. Ishizaka, R. Arita, and S. Ishiwata, Competing spin modulations in the magnetically frustrated semimetal  $\text{EuCuSb}$ , *Phys. Rev. B* **102**, 174425 (2020).
- [7] T. Kurumaji, M. Gen, S. Kitou, H. Sagayama, A. Ikeda, and T. Arima, Anisotropic magnetotransport properties coupled with spiral spin modulation in a magnetic semimetal  $\text{EuZnGe}$ , *Phys. Rev. Mater.* **6**, 094410 (2022).
- [8] J.-R. Soh, I. S.-Ramírez, X. Yang, J. Sun, I. Zivkovic, J. A. R.-Velamazán, O. Fabelo, A. Stunault, A. Bombardi, C. Balz, M. D. Le, H. C. Walker, J. H. Dil, D. Prabhakaran, H. M. Rønnow, F. de Juan, M. G. Vergniory, and A. T. Boothroyd, Weyl metallic state induced by helical magnetic order, *npj Quantum Mater.* **9**, 7 (2024).
- [9] K. Kaneko, M. D. Frontzek, M. Matsuda, A. Nakao, K. Munakata, T. Ohhara, M. Kakihana, Y. Haga, M. Hedo, T. Nakama, and Y. Ōnuki, Unique Helical Magnetic Order and Field-Induced Phase in Trillium Lattice Antiferromagnet  $\text{EuPtSi}$ , *J. Phys. Soc. Jpn.* **88**, 013702 (2019).
- [10] R. Takagi, N. Matsuyama, V. Ukleev, L. Yu, J. S. White, S. Francoual, J. R. L. Mardegan, S. Hayami, H. Saito, K. Kaneko, K. Ohishi, Y. Ōnuki, T. Arima, Y. Tokura, T. Nakajima, and S. Seki, *Nat. Commun.* **13**, 1472 (2022).
- [11] M. Gen, R. Takagi, Y. Watanabe, S. Kitou, H. Sagayama, N. Matsuyama, Y. Kohama, A. Ikeda, Y. Ōnuki, T. Kurumaji, T. Arima, and S. Seki, Rhombic skyrmion lattice coupled with orthorhombic structural distortion in  $\text{EuAl}_4$ , *Phys. Rev. B* **107**, L020410 (2023).
- [12] D. Singh, Y. Fujishiro, S. Hayami, S. H. Moody, T. Nomoto, P. R. Baral, V. Ukleev, R. Cubitt, N.-J. Steinke, D. J. Gawryluk, E. Pomjakushina, Y. Ōnuki, R. Arita, Y. Tokura, N. Kanazawa, and J. S. White, Transition between distinct hybrid skyrmion textures through their hexagonal-to-square crystal transformation in a polar magnet, *Nat. Commun.* **14**, 8050 (2023).
- [13] T. Matsumura, K. Kurauchi, M. Tsukagoshi, N. Higa, H. Nakao, M. Kakihana, M. Hedo, T. Nakama, Y. Ōnuki, Distorted triangular skyrmion lattice in a noncentrosymmetric tetragonal magnet, [arXiv:2306.14767](https://arxiv.org/abs/2306.14767).
- [14] J. Jiang and S. M. Kauzlarich, Colossal Magnetoresistance in a Rare Earth Zintl Compound with a New Structure Type:  $\text{EuIn}_2\text{P}_2$ , *Chem. Mater.* **18**, 435 (2006).
- [15] J.-Z. Ma, S. M. Nie, C. J. Yi, J. Jandke, T. Shang, M. Y. Yao, M. Naamneh, L. Q. Yan, Y. Sun, A. Chikina, *et al.*, Spin Fluctuation Induced Weyl Semimetal State in the Paramagnetic Phase of  $\text{EuCd}_2\text{As}_2$ , *Sci. Adv.* **5**, eaaw4718 (2019).
- [16] H. Su, B. Gong, W. Shi, H. Yang, H. Wang, W. Xia, Z. Yu, P.-J. Guo, J. Wang, L. Ding, L. Xu, X. Li, X. Wang, Z. Zou, N. Yu, Z. Zhu, Y. Chen, Z. Liu, K. Liu, G. Li, and Y. Guo, Magnetic exchange induced Weyl state in a semimetal  $\text{EuCd}_2\text{Sb}_2$ , *APL Mater.* **8**, 011109 (2020).
- [17] Z.-C. Wang, J. D. Rogers, X. Yao, R. Nichols, K. Atay, B. Xu, J. Franklin, I. Sochnikov, P. J. Ryan, D. Haskel, and F. Taft, Colossal Magnetoresistance without Mixed Valence in a Layered Phosphide Crystal, *Adv. Mater.* **33**, 2005755 (2021).
- [18] J. Blawat, M. Marshall, J. Singleton, E. Feng, H. Cao, W. Xie, and R. Jin, Unusual Electrical and Magnetic Properties in Layered  $\text{EuZn}_2\text{As}_2$ , *Adv. Quantum Tech.* **5**, 2200012 (2022).
- [19] S. Krebber, M. Kopp, C. Garg, K. Kummer, J. Sichelschmidt, S. Schulz, G. Poelchen, M. Mende, A. V. Virovets, K. Warawa, M. D. Thomson, A. V. Tarasov, D. Yu. Usachov, D. V. Vyalikh, H. G. Roskos, J. Müller, C. Krellner, and K. Kliemt, Colossal magnetoresistance in  $\text{EuZn}_2\text{P}_2$  and its electronic and magnetic structure, *Phys. Rev. B* **108**, 045116 (2023).
- [20] G. Cuono, R. M. Sattigeri, C. Autieri, and T. Dietl, *Ab initio* overestimation of the topological region in Eu-based compounds, *Phys. Rev. B* **108**, 075150 (2023).
- [21] A. M. Essin, J. E. Moore, and D. Vanderbilt, Magnetoelectric polarizability and axion electrodynamics in crystalline insulators, *Phys. Rev. Lett.* **102**, 146805 (2009).
- [22] Y. Xu, Z. Song, Z. Wang, H. Weng, and X. Dai, Higher-Order Topology of the Axion Insulator  $\text{EuIn}_2\text{As}_2$ , *Phys. Rev. Lett.* **122**, 256402 (2019).
- [23] Y. Tokura, K. Yasuda, and A. Tsukazaki, Magnetic topological insulators, *Nat. Rev. Phys.* **1**, 126 (2019).
- [24] B. A. Bernevig, C. Felser, and H. Beidenkopf, Progress and prospects in magnetic topological materials, *Nature* **603**, 41 (2022).
- [25] K. M. Fijalkowski, N. Liu, M. Hartl, M. Winnerlein, P. Mandal, A. Coschizza, A. Fothergill, S. Grauer, S. Schreyeck, K. Brunner, M. Greiter, R. Thomale, C. Gould, and L. W. Molenkamp, Any axion insulator must be a bulk three-dimensional topological insulator, *Phys. Rev. B* **103**, 235111 (2021).
- [26] X. Wan, A. M. Turner, A. Vishwanath, and S. Y. Savrasov, Topological semimetal and Fermi-arc surface states in the electronic structure of pyrochlore iridates, *Phys. Rev. B* **83**, 205101 (2011).
- [27] M. Mogi, M. Kawamura, R. Yoshimi, A. Tsukazaki, Y. Kozuka, N. Shirakawa, K. S. Takahashi, M. Kawasaki, and Y. Tokura, A magnetic heterostructure of topological insulators as a candidate for an axion insulator, *Nat. Mater.* **16**, 516 (2017).

- [28] D. Zhang, M. Shi, T. Zhu, D. Xing, H. Zhang, and J. Wang, Topological Axion States in the Magnetic Insulator  $\text{MnBi}_2\text{Te}_4$  with the Quantized Magnetolectric Effect, Intrinsic magnetic topological insulators in van der Waals layered  $\text{MnBi}_2\text{Te}_4$ -family materials, *Phys. Rev. Lett.* **122**, 206401 (2019).
- [29] J. Li, Y. Li, S. Du, Z. Wang, B.-L. Gu, S.-C. Zhang, K. He, W. Duan, and Y. Xu, *Sci. Adv.* **5**, eaaw5685 (2019).
- [30] Y. Deng, Y. Yu, M. Z. Shi, Z. Guo, Z. Xu, J. Wang, X. H. Chen, Y. Zhang, Quantum anomalous Hall effect in intrinsic magnetic topological insulator  $\text{MnBi}_2\text{Te}_4$ , *Science* **367**, 895 (2020).
- [31] A. M. Goforth, P. Klavins, J. C. Fettinger, and S. M. Kauzlarich, Magnetic Properties and Negative Colossal Magnetoresistance of the Rare Earth Zintl phase  $\text{EuIn}_2\text{As}_2$ , *Inorg. Chem.* **47**, 11048 (2008).
- [32] Y. Zhang, K. Deng, X. Zhang, M. Wang, Y. Wang, C. Liu, J.-W. Mei, S. Kumar, E. F. Schwier, K. Shimada, C. Chen, and B. Shen, In-plane antiferromagnetic moments and magnetic polaron in the axion topological insulator candidate  $\text{EuIn}_2\text{As}_2$ , *Phys. Rev. B* **101**, 205126 (2020).
- [33] T. Sato, Z. Wang, D. Takane, S. Souma, C. Cui, Y. Li, K. Nakayama, T. Kawakami, Y. Kubota, C. Cacho, T. K. Kim, A. Arab, V. N. Strocov, Y. Yao, and T. Takahashi, Signature of band inversion in the antiferromagnetic phase of axion insulator candidate  $\text{EuIn}_2\text{As}_2$ , *Phys. Rev. Res.* **2**, 033342 (2020).
- [34] S. Regmi, M. M. Hosen, B. Ghosh, B. Singh, G. Dhakal, C. Sims, B. Wang, F. Kabir, K. Dimitri, Y. Liu, A. Agarwal, H. Lin, D. Kaczorowski, A. Bansil, and M. Neupane, Temperature-dependent electronic structure in a higher-order topological insulator candidate  $\text{EuIn}_2\text{As}_2$ , *Phys. Rev. B* **102**, 165153 (2020).
- [35] F. H. Yu, H. M. Mu, W. Z. Zhuo, Z. Y. Wang, Z. F. Wang, J. J. Ying, and X. H. Chen, Elevating the magnetic exchange coupling in the compressed antiferromagnetic axion insulator candidate  $\text{EuIn}_2\text{As}_2$ , *Phys. Rev. B* **102**, 180404(R) (2020).
- [36] M. Gong, D. Sar, J. Friedman, D. Kaczorowski, S. A. Razek, W.-C. Lee, and P. Aynajian, Surface state evolution induced by magnetic order in axion insulator candidate  $\text{EuIn}_2\text{As}_2$ , *Phys. Rev. B* **106**, 125156 (2022).
- [37] J. Yan, Z. Z. Jiang, R. C. Xiao, W. J. Lu, W. H. Song, X. B. Zhu, X. Luo, Y. P. Sun, and M. Yamashita, Field-induced topological Hall effect in antiferromagnetic axion insulator candidate  $\text{EuIn}_2\text{As}_2$ , *Phys. Rev. Research* **4**, 013163 (2022).
- [38] Q. Wu, T. Hu, D. Wu, R. Li, L. Yue, S. Zhang, S. Xu, Q. Liu, T. Dong, and N. Wang, Spin dynamics in the axion insulator candidate  $\text{EuIn}_2\text{As}_2$ , *Phys. Rev. B* **107**, 174411 (2023).
- [39] S. X. M. Riberolles, T. V. Trevisan, B. Kuthanazhi, T. W. Heitmann, F. Ye, D. C. Johnston, S. L. Bud'ko, D. H. Ryan, P. C. Canfield, A. Kreyssig, A. Vishwanath, R. J. McQueeney, L.-L. Wang, P. P. Orth, and B. G. Ueland, Magnetic crystalline-symmetry-protected axion electrodynamics and field-tunable unpinned Dirac cones in  $\text{EuIn}_2\text{As}_2$ , *Nat. Commun.* **12**, 999 (2021).
- [40] J.-R. Soh, A. Bombardi, F. Mila, M. C. Rahn, D. Prabhakaran, S. Francoual, H. M. Rønnow, and A. T. Boothroyd, Understanding unconventional magnetic order in a candidate axion insulator by resonant elastic x-ray scattering, *Nat. Commun.* **14**, 3387 (2023).
- [41] E. Donoway, T. V. Trevisan, A. Liebman - Peláez, R. P. Day, K. Yamakawa, Y. Sun, J. R. Soh, D. Prabhakaran, A. Boothroyd, R. M. Fernandes, J. G. Analytis, J. E. Moore, J. Orenstein, and V. Sunko, Symmetry-breaking pathway towards the unpinned broken helix, arXiv:2310.16018.
- [42] See Supplemental Material at xxxx for details of the experiments and analyses, which includes Refs. [43–45].
- [43] F. Izumi and K. Momma, Three-Dimensional Visualization in Powder Diffraction, *Solid State Phenom.* **130**, 15 (2007).
- [44] CrysAlisPro (Agilent Technologies Ltd, Yarnton, 2014).
- [45] V. Petříček, M. Dušek, and L. Palatinus, Crystallographic computing system JANA2006: General features, *Z. Kristallogr. Cryst. Mater.* **229**, 345 (2014).
- [46] T. Kosugia, S. Kawanob, N. Achiwac, A. Onoderad, Y. Nakaie, and N. Yamamoto, Direct evidence of helifan structures in holmium by single crystal neutron diffraction, *Physica B* **334**, 365 (2003).
- [47] N. J. Ghimire, R. L. Dally, L. Poudel, D. C. Jones, D. Michel, N. Thapa Magar, M. Bleuel, M. A. McGuire, J. S. Jiang, J. F. Mitchell, J. W. Lynn, I. I. Mazin, Competing magnetic phases and fluctuation-driven scalar spin chirality in the kagome metal  $\text{YMn}_6\text{Sn}_6$ , *Sci. Adv.* **6**, eabe2680 (2020).
- [48] In the case of  $q_{1z} = 1/3$ , the high-harmonic  $\mathbf{Q}_2 - 2\mathbf{Q}_1$  and  $3\mathbf{Q}_1$  positions accidentally overlap with the  $\mathbf{Q}_1$  and  $\mathbf{Q}_2$  positions, respectively.
- [49] S. Hayami, R. Ozawa, and Y. Motome, Effective bilinear-biquadratic model for noncoplanar ordering in itinerant magnets, *Phys. Rev. B* **95**, 224424 (2017).

## Supplemental Material for “Incommensurate broken-helix and broken-fanlike states in axion insulator candidate $\text{EuIn}_2\text{As}_2$ ”

Masaki Gen,<sup>1,\*</sup> Yukako Fujishiro,<sup>1</sup> Kazuki Okigami,<sup>2</sup> Satoru Hayami,<sup>3</sup> Kiyohiro Adachi,<sup>4</sup> Daisuke Hashizume,<sup>4</sup>  
Takashi Kurumaji,<sup>5,6</sup> Hajime Sagayama,<sup>7</sup> Hironori Nakao,<sup>7</sup> Yoshinori Tokura,<sup>1,2,8</sup> and Taka-hisa Arima<sup>1,5</sup>

<sup>1</sup>*RIKEN Center for Emergent Matter Science (CEMS), Wako 351-0198, Japan*

<sup>2</sup>*Department of Applied Physics, University of Tokyo, Tokyo 113-8656, Japan*

<sup>3</sup>*Graduate School of Science, Hokkaido University, Sapporo 060-0810, Japan*

<sup>4</sup>*Materials Characterization Support Team, RIKEN Center for Emergent Matter Science (CEMS), Wako 351-0198, Japan*

<sup>5</sup>*Department of Advanced Materials Science, University of Tokyo, Kashiwa 277-8561, Japan*

<sup>6</sup>*Division of Physics, Mathematics and Astronomy, California Institute of Technology, Pasadena, California 91125, USA*

<sup>7</sup>*Institute of Materials Structure Science, High Energy Accelerator Research Organization, Tsukuba 305-0801, Japan*

<sup>8</sup>*Tokyo College, University of Tokyo, Tokyo 113-8656, Japan*

This Supplemental Material includes contents as listed below:

- Note 1. Single-crystal growth and characterization
- Note 2. Powder XRD measurement at low temperatures
- Note 3. Single-crystal XRD measurement for samples #1 and #2
- Note 4. Sample and strain dependence of RXS profiles at 5 K in zero field
- Note 5. Polarization analysis for the RXS data at 5 K
- Note 6. Calculation of spin structural factors based on the broken-helix state
- Note 7. Comparison of the amplitude of the  $\mathbf{Q}_1$  and  $\mathbf{Q}_2$  modulations
- Note 8. Theoretical calculation based on a bilinear-biquadratic model in real space

### Note 1. Single-crystal growth and characterization

Single crystals of  $\text{EuIn}_2\text{As}_2$  were grown by an indium flux method. The chunks of Eu, In, and As were weighed with a molar ratio of 3:36:9 (2.5–3.0 g total weight) and placed in alumina crucibles, which were then sealed in a fused silica tube. The sample was heated up to 900 °C over 1 day, followed by a 2 hours dwell time. It was then cooled down to 770 °C over 48 hours, at which point the excess indium flux was removed by a centrifuge.

The sample purity was checked by the powder x-ray diffraction (XRD) measurement on crushed single crystals at room temperature, using Rigaku SmartLab diffractometer at Materials Characterization Support Team, RIKEN CEMS. The XRD patterns were recorded on a diffractometer with Bragg-Brentano geometry, and the incident x-ray beam was monochromatized by a Johansson-type monochromator with a Ge(111) crystal to select only  $\text{Cu-}K\alpha_1$  radiation. We confirm the hexagonal space group  $P6_3/mmc$  (No. 194) for the main  $\text{EuIn}_2\text{As}_2$  phase, in together with minor impurity phases of In [Space group  $I4/mmm$  (No. 139)] and InAs [Space group  $F\bar{4}3m$  (No. 216)]. The Rietveld analysis was performed using the RIETAN software [1], yielding lattice parameters  $a = b = 4.20521(4)$  Å and  $c = 17.8915(2)$  Å, in accord with Refs. [2, 3] (See Note 2 for details). The results of the powder XRD at low temperatures are described in Note 2, and those of the single-crystal XRD are described in Note 3. The magnetization was measured using a superconducting quantum interference device (MPMS, Quantum Design), confirming that the magnetization data are almost consistent with previous reports [3–6], as shown in Figs. 2(d) and 3(a) in the main text.

---

\* masaki.gen@riken.jp

## Note 2. Powder XRD measurement at low temperatures

We summarize the results of the powder XRD measurement performed between 10 and 300 K in Table S1 and Fig. S1. Neither peak splitting nor the appearance of new peaks indicative of a structural phase transition was observed below the magnetic ordering temperature  $T_{N2} = 16.2$  K, as shown in Fig. S1(d).

TABLE S1. Structural parameters of  $\text{EuIn}_2\text{As}_2$  at 300 K (top) and 10 K (bottom) obtained from the powder XRD measurements on crushed single crystals. The hexagonal  $P6_3/mmc$  space group is assumed. Reliability factors are shown in the inset of Figs. S1(a) and S1(c).

$T = 300 \text{ K } (a = 4.20521(10) \text{ \AA}, c = 17.89150(32) \text{ \AA})$						
Site	Symmetry	Occupancy	$x$	$y$	$z$	$U (\text{\AA}^2)$
Eu	$2a$	1 (fix)	0	0	0	0.01543(55)
In	$4f$	1 (fix)	1/3	2/3	0.32668(7)	0.01763(40)
As	$4f$	1 (fix)	2/3	1/3	0.39276(11)	0.01577(53)
$T = 10 \text{ K } (a = 4.19712(5) \text{ \AA}, c = 17.83751(25) \text{ \AA})$						
Site	Symmetry	Occupancy	$x$	$y$	$z$	$U (\text{\AA}^2)$
Eu	$2a$	1 (fix)	0	0	0	0.00961(48)
In	$4f$	1 (fix)	1/3	2/3	0.32721(7)	0.00858(34)
As	$4f$	1 (fix)	2/3	1/3	0.39260(11)	0.00700(47)

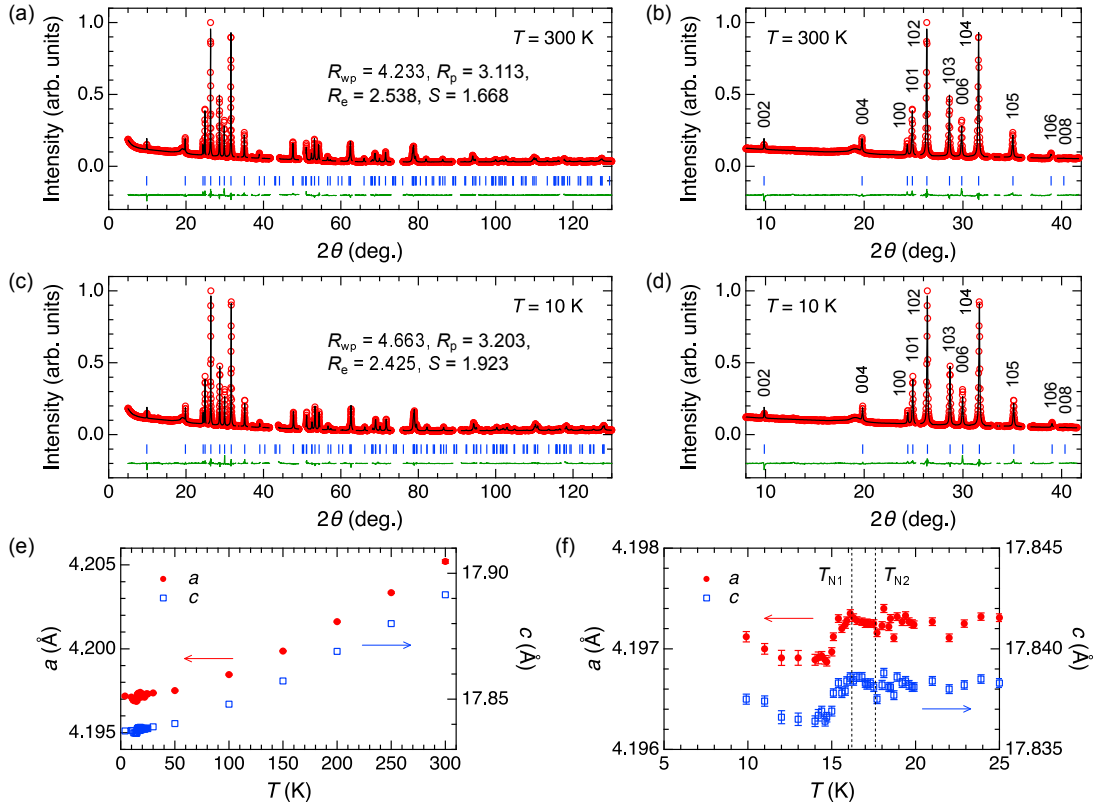


FIG. S1. [(a)–(d)] Powder XRD patterns and structural refinements of  $\text{EuIn}_2\text{As}_2$  at (a) 300 K and (c) 10 K. Panels (b) and (d) display enlarged views of panels (a) and (c), respectively. The open red circles indicate the experimental data. The overlapped black curves indicate the calculated patterns with the hexagonal  $P6_3/mmc$  space group as the main phase. Additional peaks originating from impurity phases and the background of a copper substrate were excluded ( $2\theta \sim 42^\circ, 50^\circ, 55^\circ, 59^\circ, 63^\circ, 67^\circ, 75^\circ, 90^\circ, 95^\circ, 117^\circ$ ). The vertical bars indicate the positions of the Bragg reflections. The bottom curves show the difference between the experimental and calculated intensities. [(e)(f)] Temperature dependence of the lattice constants  $a$  (left axis) and  $c$  (right axis) obtained from the Rietveld analysis. Panel (f) is an enlarged view of panel (e) at low temperatures.



### Note 3. Single-crystal XRD measurement for samples #1 and #2

We performed single-crystal XRD measurements on two pieces of  $\text{EuIn}_2\text{As}_2$  samples (#1 and #2), which were obtained from the same batch and used for the resonant x-ray scattering (RXS) experiments. The data were recorded on Rigaku MicroMax<sup>TM</sup>-007HF diffractometer equipped with a HyPix-6000 detector using Mo  $K_\alpha$  radiation ( $\lambda = 0.70926 \text{ \AA}$ ) at room temperature. The intensities of Bragg reflections were collected by the CrysAlisPro software [7]. Here, we employed absorption corrections based on the actual crystal size and shape for each sample in the finalization process. The crystal structures were refined by the Jana2006 software [8].

All the structural parameters and crystallographic data are summarized in Tables S2–S4. When optimizing the structural parameters, the occupancy of the Eu site was refined with fixing those of the In and As sites to 1. As shown in Tables S2 and S3, a Eu deficiency is found to 1.6(5)% for sample #1 and 1.1(4)% for sample #2. We confirm that there is no defect at In and As sites from the structural analysis with independently relaxing the occupancy of these sites.

TABLE S2. Structural parameters of  $\text{EuIn}_2\text{As}_2$  (sample #1) at 300 K. The space group is  $P6_3/mmc$  (No. 194), and the lattice parameters are  $a = b = 4.210075(53) \text{ \AA}$ ,  $c = 17.911096(254) \text{ \AA}$ ,  $\alpha = \beta = 90^\circ$ ,  $\gamma = 120^\circ$ .

Site	Symmetry	Occupancy	$x$	$y$	$z$	$U_{11}(=U_{22}) (\text{\AA}^2)$	$U_{33} (\text{\AA}^2)$	$U_{12} (\text{\AA}^2)$
Eu	$2a$	0.9836(46)	0	0	0	0.008504(138)	0.012646(213)	0.004252(69)
In	$4f$	1 (fix)	1/3	2/3	0.327193(26)	0.010401(139)	0.009377(174)	0.005200(70)
As	$4f$	1 (fix)	2/3	1/3	0.392478(39)	0.007285(172)	0.009782(256)	0.003643(86)

TABLE S3. Structural parameters of  $\text{EuIn}_2\text{As}_2$  (sample #2) at 300 K. The space group is  $P6_3/mmc$  (No. 194), and the lattice parameters are  $a = b = 4.210541(51) \text{ \AA}$ ,  $c = 17.922931(227) \text{ \AA}$ ,  $\alpha = \beta = 90^\circ$ ,  $\gamma = 120^\circ$ .

Site	Symmetry	Occupancy	$x$	$y$	$z$	$U_{11}(=U_{22}) (\text{\AA}^2)$	$U_{33} (\text{\AA}^2)$	$U_{12} (\text{\AA}^2)$
Eu	$2a$	0.9890(39)	0	0	0	0.010279(98)	0.011567(130)	0.005140(49)
In	$4f$	1 (fix)	1/3	2/3	0.327150(19)	0.011983(99)	0.009045(109)	0.005991(49)
As	$4f$	1 (fix)	2/3	1/3	0.392463(29)	0.008805(121)	0.009645(165)	0.004402(61)

TABLE S4. Summary of crystallographic data of  $\text{EuIn}_2\text{As}_2$  (samples #1 and #2).

	Sample #1	Sample #2
Temperature (K)	300	300
Wavelength ( $\text{\AA}$ )	0.70926	0.70926
Crystal dimension ( $\mu\text{m}^3$ )	$190 \times 140 \times 60$	$250 \times 150 \times 50$
Space group	$P6_3/mmc$	$P6_3/mmc$
$a$ ( $\text{\AA}$ )	4.210075(53)	4.210541(51)
$c$ ( $\text{\AA}$ )	17.911096(254)	17.922931(227)
$Z$	2	2
$F(000)$	451.93	452.61
$(\sin \theta/\lambda)_{\text{max}}$ ( $\text{\AA}^{-1}$ )	1.28	1.28
$N_{\text{Total}}$	26364	25288
$N_{\text{Unique}}$	970	1003
Average redundancy	27.179	25.212
Completeness (%)	96.9	100
$N_{\text{parameter}}$	11	11
$R_1$ ( $I > 3\sigma$ ) [number of reflections]	3.19% [806]	2.61% [868]
$R_1$ (all) [number of reflections]	4.27% [970]	3.52% [1003]
$wR_2$ (all) [number of reflections]	8.68% [970]	6.63% [1003]
GOF (all) [number of reflections]	4.23% [970]	3.80% [1003]

#### Note 4. Sample and strain dependence of RXS profiles at 5 K in zero field

For the resonant x-ray scattering (RXS) experiments on  $\text{EuIn}_2\text{As}_2$ , we picked up two specimens (#1 and #2) from the same batch and polished the as-grown (001) surfaces to remove the In flux. Furthermore, we cut sample #2 into two pieces (#2a and #2b). In order to verify the effect of extrinsic strain in our RXS experiments, we attached the samples to an aluminium plate in two different extreme ways; a flat (001) plane was homogeneously glued using GE vanish for sample #1 and #2a, whereas only the two short sides facing each other along the  $b$  axis were fixed to the Al plate for sample #2b, as indicated by red arrows in Fig. S2(a). As shown in Fig. S1(e), the powder XRD reveals that the thermal shrinkage of the  $ab$  plane of  $\text{EuIn}_2\text{As}_2$  from room temperature to 10 K is approximately 0.2 %, which is significantly small compared to that of the Al ( $\sim 0.7$  %). Accordingly, a compressive strain was expected to be applied along the  $b$  axis for sample #2b.

In Fig. S2(b), we show the RXS profiles obtained in the  $(0, 0, L)$  scan at 5 K and 30 K in zero field for the three samples. Two kinds of magnetic Bragg peaks,  $\mathbf{Q}_1 = (0, 0, q_{1z})$  and  $\mathbf{Q}_2 = (0, 0, 1)$ , are commonly observed for all the samples. However, there are differences in the  $q_{1z}$  value as well as the intensity ratio of the  $\mathbf{Q}_1$  and  $\mathbf{Q}_2$  peaks ( $I_{\mathbf{Q}_1}/I_{\mathbf{Q}_2}$ ) between samples #1 and #2a:  $q_{1z} = 0.290$  and  $I_{\mathbf{Q}_1}/I_{\mathbf{Q}_2} = 0.095$  for sample #1, while  $q_{1z} = 0.253$  and  $I_{\mathbf{Q}_1}/I_{\mathbf{Q}_2} = 0.011$  for sample #2a. The broader width of the  $\mathbf{Q}_1$  peak compared to the  $\mathbf{Q}_2$  peak for sample #1 would be due to spatial variation of the  $q_{1z}$  inside the sample. Notably, we find that the  $q_{1z}$  value does not significantly change by applying thermal strain, as evidenced by the observation of  $q_{1z} = 0.260$  for sample #2b. From these results, we conclude that the observed variability in  $q_{1z}$  is primarily attributed to the sample dependence rather than extrinsic strain. In Note 3, we show the evidence of a slight difference in the sample stoichiometry between samples #1 and #2 revealed by the single-crystal XRD measurement.

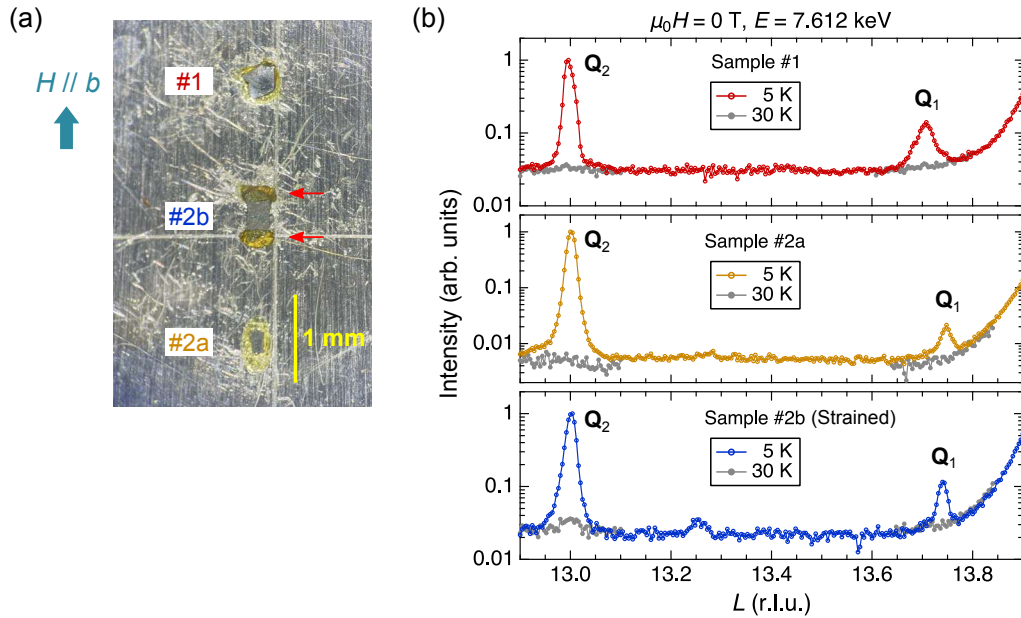


FIG. S2. (a) Photograph of  $\text{EuIn}_2\text{As}_2$  single crystals (#1, #2b, and #2a from the top), which are glued on an aluminium plate for the RXS experiments. (b) RXS profiles in the  $(0, 0, L)$  scan at 5 K and 30 K in zero field for samples #1 (top), #2b (middle), and #2a (bottom). The left axis is plotted logarithmically. The data for sample #1 is identical with that shown in Fig. 2(c) in the main text.

### Note 5. Polarization analysis for the RXS data at 5 K

In order to reveal the orientation of the  $\mathbf{Q}_1$  and  $\mathbf{Q}_2$  modulations in the zero-field low-temperature (LT) phase below  $T_{N1} = 16.2$  K and the high-field (HF) phase above  $\mu_0 H_{c1} = 0.2$  T with  $H \parallel b$ , we performed polarization analysis at 5 K using incident x-rays in resonance with the Eu  $L_2$  absorption edge (7.612 keV). As described in the main text, the magnetic scattering intensity  $I$  is given by  $I \propto (\mathbf{e}_i \times \mathbf{e}_f) \cdot \mathbf{m}_Q$ , where  $\mathbf{e}_i$  ( $\mathbf{e}_f$ ) is the polarization vector of the incident (scattered) beam, and  $\mathbf{m}_Q$  is a spin moment for the  $\mathbf{Q}$  modulation. The  $\pi$ - $\pi'$  channel ( $I_{\pi-\pi'}$ ) always detects the modulated component along  $b$  ( $m_b$ ), and the  $\pi$ - $\sigma'$  channel ( $I_{\pi-\sigma'}$ ) detects those along  $a^*$  ( $m_{a^*}$ ) and  $c$  ( $m_c$ ). For the latter, the intensity ratio of  $m_{a^*}$  and  $m_c$  is given by  $\cos^2 \omega : \sin^2 \omega$ , where  $\omega$  corresponds to the angle between the propagation vector of the incident beam ( $\mathbf{k}_i$ ) and the  $a^*$  axis. We focused on the magnetic Bragg spots at  $(-2, 0, 11.71)$  and  $(2, 0, 11.71)$  for analyzing the  $\mathbf{Q}_1$  modulation and those at  $(0, 0, 9)$  and  $(0, 0, 17)$  for the  $\mathbf{Q}_2$  modulation.

Notably,  $\omega$  is close to  $0^\circ$  and  $90^\circ$  for the  $(-2, 0, 11.71)$  and  $(2, 0, 11.71)$  positions, respectively. We can hence independently extract information on  $m_{a^*}$  and  $m_c$  of the  $\mathbf{Q}_1$  modulation by measuring  $I_{\pi-\sigma'}$  at  $(-2, 0, 11.71)$  and  $(2, 0, 11.71)$ , respectively [Figs. S3(a) and S3(b)]. As shown in Figs. S3(h)–S3(j),  $I_{\pi-\sigma'}$  exhibits no intensity in all the RXS profiles, indicating the absence of  $m_c$  of the  $\mathbf{Q}_1$  modulation in both the LT and HF phases. As for the  $\mathbf{Q}_2$  peaks,  $\omega$  is  $24.2^\circ$  for  $(0, 0, 9)$  and  $50.7^\circ$  for  $(0, 0, 17)$ . Accordingly, 83 % of  $m_{a^*}$  and 17 % of  $m_c$  components contribute to  $I_{\pi-\sigma'}$  at  $(0, 0, 9)$ , and 40 % of  $m_{a^*}$  and 60 % of  $m_c$  components contribute to  $I_{\pi-\sigma'}$  at  $(0, 0, 17)$ . At 0 T, the observed intensity ratio between the  $\pi$ - $\pi'$  and  $\pi$ - $\sigma'$  channels is  $I_{\pi-\sigma'}/I_{\pi-\pi'} \approx 0.8$  at  $(0, 0, 9)$  [Fig. S3(k)] and  $I_{\pi-\sigma'}/I_{\pi-\pi'} \approx 0.3$  at  $(0, 0, 17)$  [Fig. S3(n)]. The difference in  $I_{\pi-\sigma'}/I_{\pi-\pi'}$  should be attributed to the difference in the contribution from  $m_{a^*}$  of the  $\mathbf{Q}_2$  modulation. In other words,  $m_c$  of the  $\mathbf{Q}_2$  modulation should be absent in the LT phase. This tendency also holds at 0.1 T:  $I_{\pi-\sigma'}/I_{\pi-\pi'} \approx 7$  at  $(0, 0, 9)$  [Fig. S3(l)] and  $I_{\pi-\sigma'}/I_{\pi-\pi'} \approx 1.5$  at  $(0, 0, 17)$  [Fig. S3(o)]. After the metamagnetic transition,  $I_{\pi-\sigma'}$  have no intensity at both  $(0, 0, 9)$  and  $(0, 0, 17)$ , indicating the absence of  $m_c$  as well as  $m_{a^*}$  of the  $\mathbf{Q}_2$  modulation in the HF phase. From the above considerations, we can conclude that all the spins lie within the  $ab$  plane in the magnetic ordering phases in  $\text{EuIn}_2\text{As}_2$ .

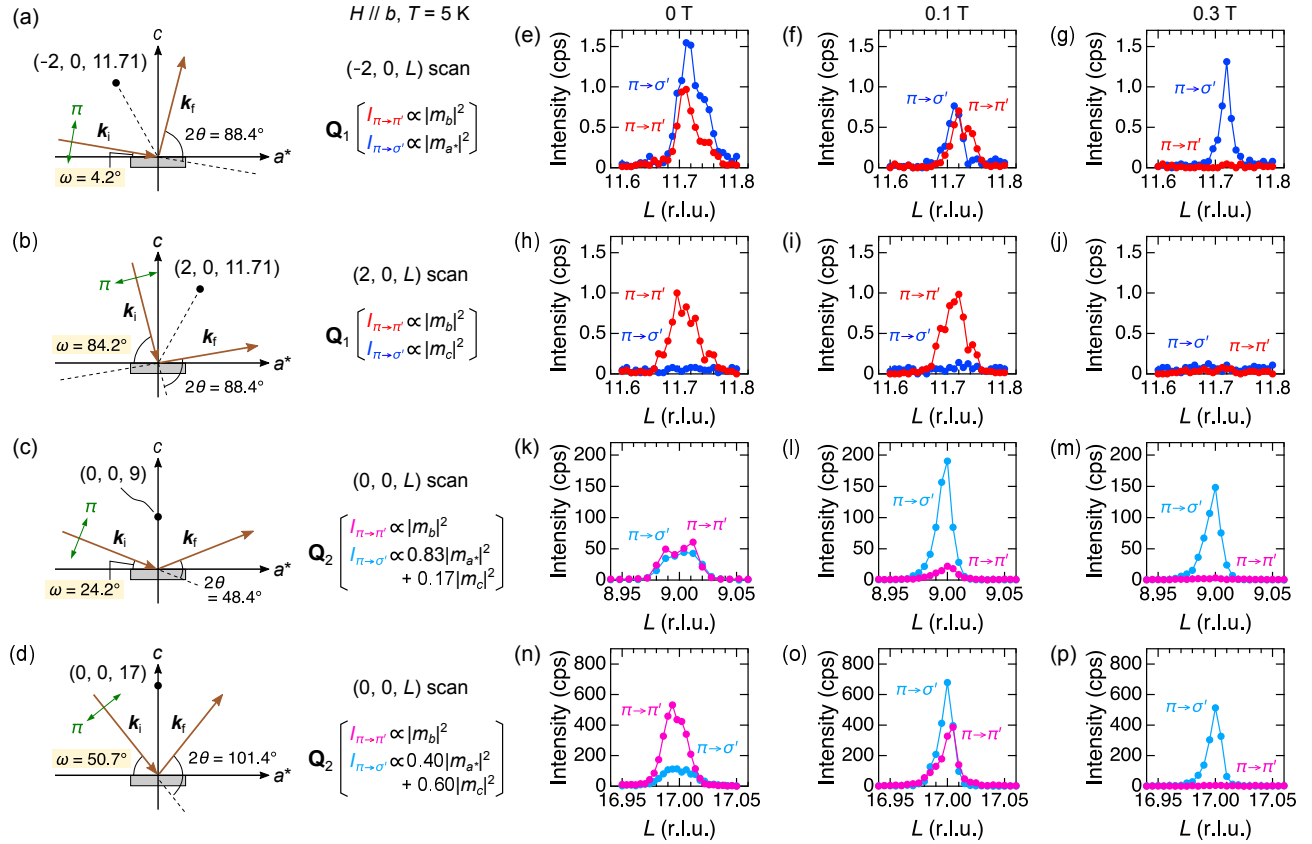


FIG. S3. [(a)–(d)] Experimental configuration of the RXS focusing on the magnetic Bragg spots at (a)  $(-2, 0, 11.71)$ , (b)  $(2, 0, 11.71)$ , (c)  $(0, 0, 9)$ , and (d)  $(0, 0, 17)$ . The former (latter) two correspond to the  $\mathbf{Q}_1$  ( $\mathbf{Q}_2$ ) peak. [(e)–(p)] RXS profiles of the polarization analysis at 5 K at 0 T [(e)(h)(k)(n)], 0.1 T [(f)(i)(l)(o)], and 0.3 T [(g)(j)(m)(p)] with  $H \parallel b$ . Panels (e)–(g), (h)–(j), (k)–(m), and (n)–(p) show the data of the  $(-2, 0, L)$  scan around  $L = 11.71$ ,  $(2, 0, L)$  scan around  $L = 11.71$ ,  $(0, 0, L)$  scan around  $L = 9$ , and  $(0, 0, L)$  scan around  $L = 17$ , respectively.

## Note 6. Calculation of spin structural factors based on the broken-helix state

As discussed in the main text, the LT phase is identified as a broken-helix state with a superposition of incommensurate helical  $\mathbf{Q}_1$  and AFM  $\mathbf{Q}_2$  modulations from our RXS data [Fig. S4(a)]. Accordingly, the magnetic structure can be approximately described as  $\mathbf{m}(\mathbf{r}_i) \propto (1, i, 0) \sum_{\eta=1,2} m_{\mathbf{Q}_\eta} \exp(i\mathbf{Q}_\eta \cdot \mathbf{r}_i) + \text{c.c.}$  in zero field. Under an equal moment-size condition, i.e.,  $\mathbf{S}_i = \mathbf{m}(\mathbf{r}_i)/|\mathbf{m}(\mathbf{r}_i)|$ , we calculate the spin structure factor, defined as  $S(\mathbf{q}) = (1/N) \sum_{i,j} \langle \mathbf{S}_i \cdot \mathbf{S}_j \rangle e^{i\mathbf{q}(\mathbf{r}_i - \mathbf{r}_j)}$ , at  $\mathbf{Q}_1$  and  $\mathbf{Q}_2$  as well as at higher-harmonic  $\mathbf{Q}_2 - 2\mathbf{Q}_1$  and  $3\mathbf{Q}_1$  positions. Note that  $S(\mathbf{q}) = 0$  at other  $\mathbf{Q}$  positions for an infinite number of spins,  $N \rightarrow \infty$ . Figures S4(b) and S4(c) show a  $m_{\mathbf{Q}_1}/m_{\mathbf{Q}_2}$  dependence of  $S(\mathbf{Q}_1)/S(\mathbf{Q}_2)$ ,  $S(\mathbf{Q}_2 - 2\mathbf{Q}_1)/S(\mathbf{Q}_2)$ , and  $S(3\mathbf{Q}_1)/S(\mathbf{Q}_2)$ . The  $S(\mathbf{q})$  profiles exhibit an anomaly at a singular point  $m_{\mathbf{Q}_1}/m_{\mathbf{Q}_2} = 1$ , where the antiparallel  $m_{\mathbf{Q}_1}$  and  $m_{\mathbf{Q}_2}$  moments cancel each other out. In Note 7, we estimate  $m_{\mathbf{Q}_1}/m_{\mathbf{Q}_2}$  by comparing Fig. S4(b) with the observed intensities of the  $\mathbf{Q}_1$  and  $\mathbf{Q}_2$  peaks.

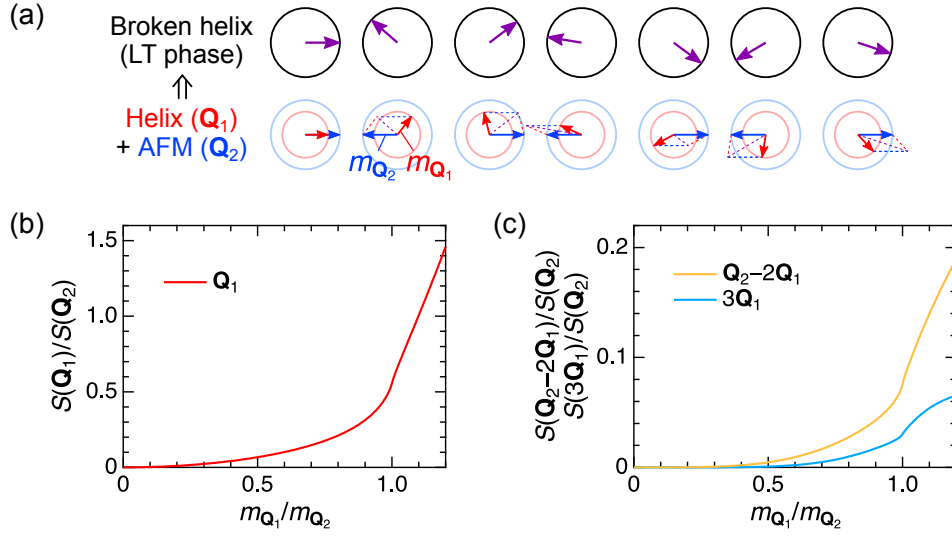


FIG. S4. (a) Schematic of the broken-helix state, composed of the incommensurate helical  $\mathbf{Q}_1$  and AFM  $\mathbf{Q}_2$  modulations with a magnitude of  $m_{\mathbf{Q}_1}$  and  $m_{\mathbf{Q}_2}$ , respectively. [(b)(c)]  $m_{\mathbf{Q}_1}/m_{\mathbf{Q}_2}$  dependence of the spin structure factor  $S(\mathbf{q})$  relative to  $S(\mathbf{Q}_2)$  at (b)  $\mathbf{Q}_1$ , (c)  $\mathbf{Q}_2 - 2\mathbf{Q}_1$  and  $3\mathbf{Q}_1$ .

## Note 7. Comparison of the amplitude of the $\mathbf{Q}_1$ and $\mathbf{Q}_2$ modulations

In Fig. 1(b) of the main text, we compare the ratio of the magnetic-moment amplitude of the  $\mathbf{Q}_1$  and  $\mathbf{Q}_2$  modulations,  $m_{\mathbf{Q}_1}/m_{\mathbf{Q}_2}$ , among four samples; two (samples #1 and #2) were measured in our RXS experiments, and the other two were measured in the previous RXS experiment by Soh *et al.* [5] and the neutron diffraction (ND) experiment by Riberolles *et al.* [6]. In this section, we show how  $m_{\mathbf{Q}_1}/m_{\mathbf{Q}_2}$  is estimated for each experimental data.

### Our RXS data

First, we estimate the intensity ratio of the  $00L$  reflections with  $L = 13.71$  and  $L = 13$  in the RXS profile at 5 K in zero field for each sample [see the top and middle panels in Fig. S2(b)]. From the Gaussian fit on each peak, we obtain  $I_{\mathbf{Q}_1}/I_{\mathbf{Q}_2} = 0.1743$  for sample #1 and  $I_{\mathbf{Q}_1}/I_{\mathbf{Q}_2} = 0.0123$  for sample #2 (#2a). We here note again that the magnetic scattering intensity is given by  $I \propto |(\mathbf{e}_i \times \mathbf{e}_f) \cdot \mathbf{m}_{\mathbf{Q}}|^2$ . Accordingly, a  $\mathbf{Q}$ -dependent correction factor should be applied to the observed peak intensity. As mentioned in Note. 5, the  $\pi - \pi'$  channel detects the  $m_b$  component, while the  $\pi - \sigma'$  channel detects the  $m_{a^*}$  component (the absence of  $m_c$  is confirmed). Assuming that magnetic domains of the broken helix are randomly oriented within the  $ab$  plane, the correction factor can be approximated to  $\sin^2 2\theta + \cos^2 \theta$ . In our RXS experiments, the energy of the incident x-ray was  $E = 7.612$  keV, in resonance with the Eu  $L_2$  edge, so that  $2\theta = 77.49^\circ$  for  $L = 13.71$  and  $2\theta = 72.81^\circ$  for  $L = 13$ . Then,  $\sin^2 2\theta + \cos^2 \theta$  is 1.561 for  $L = 13.71$  and 1.560 for  $L = 13$ . Using these factors, the corrected intensity ratio is  $I_{\mathbf{Q}_1}/I_{\mathbf{Q}_2} = 0.1742$  for sample #1 and 0.0123 for sample #2. Finally, we can estimate  $m_{\mathbf{Q}_1}/m_{\mathbf{Q}_2}$  from Fig. S4(b) assuming an equal-moment broken-helix state, yielding  $m_{\mathbf{Q}_1}/m_{\mathbf{Q}_2} \approx 0.75$  for sample #1 and 0.22 for sample #2.

### RXS data by Soh *et al.*

From the RXS profile at 6 K in zero field shown in Fig. 1(a) of Ref. [5], we estimate the intensity ratio of the  $00L$  reflections with  $L = 13\frac{2}{3}$  and  $L = 13$  to be 1:1.24. Importantly, as the observed  $q_{1z}$  value is 0.333 (close to 1/3), the higher-harmonic  $\mathbf{Q}_2 - 2\mathbf{Q}_1$  and  $3\mathbf{Q}_1$  peaks are expected to overlap with the  $\mathbf{Q}_1$  and  $\mathbf{Q}_2$  peaks, respectively. Therefore, one needs to take into account the higher-harmonic contributions in estimating  $m_{\mathbf{Q}_1}/m_{\mathbf{Q}_2}$ . For evaluating the correction factors, we here consider only the  $\mathbf{Q}_1$  and  $\mathbf{Q}_2$  peaks for simplicity. Since the energy of the incident x-ray was  $E = 6.975$  keV, in resonance with the Eu  $L_3$  edge,  $2\theta = 85.83^\circ$  for  $L = 13\frac{2}{3}$  and  $2\theta = 80.74^\circ$  for  $L = 13$  (We here use the lattice constant  $c = 17.83751(25)$  Å at 10 K obtained in our powder XRD measurement, as shown in Tab. S1). Therefore,  $\sin^2 2\theta + \cos^2 \theta$  is 1.531 for  $L = 13.71$  and 1.555 for  $L = 13$ . Using these correction factors and Figs. S4(b) and S4(c), we finally obtain  $m_{\mathbf{Q}_1}/m_{\mathbf{Q}_2} \approx 1.14$ .

### ND data by Riberolles *et al.*

In Supplementary Table III of Ref. [6], the authors provide intensity data for several magnetic peaks after absorption corrections. The ND experiment detects magnetic moments perpendicular to the magnetic propagation vectors. Considering that there is no magnetic moment along the  $c$  axis in  $\text{EuIn}_2\text{As}_2$ , it is straightforward to compare the  $00L$  magnetic reflections with each other because only the magnetic form factor  $f(\mathbf{Q}_\eta)$  affects the magnetic scattering intensity. Therefore, we choose six magnetic peaks for estimating  $m_{\mathbf{Q}_1}/m_{\mathbf{Q}_2}$ :  $004 - q_{1z}$ ,  $004 + q_{1z}$ ,  $006 - q_{1z}$ , and  $006 + q_{1z}$  for  $\mathbf{Q}_1$ , and  $004$  and  $006$  for  $\mathbf{Q}_2$ . Note that,  $f(\mathbf{Q}_\eta) \equiv A \exp(-as^2) + B \exp(-bs^2) + C \exp(-cs^2) + D$ , where  $A = 0.0755$ ,  $a = 25.2960$ ,  $B = 0.3001$ ,  $b = 11.5993$ ,  $C = 0.6438$ ,  $c = 4.0252$ , and  $D = -0.0196$  for the  $\text{Eu}^{2+}$  ion, and  $s = 1/2d_{hkl}$ . Using the lattice constant  $c = 17.837$  Å at 10 K (Table S1) and Fig. S4(b), we finally obtain  $m_{\mathbf{Q}_1}/m_{\mathbf{Q}_2} \approx 0.91$ .

### Note 8. Theoretical calculation based on a bilinear-biquadratic model in real space

Donoway *et al.* [9] recently demonstrated that a microscopic spin Hamiltonian, including long-range Heisenberg exchange and four-spin exchange interactions in real space, can realize a broken-helix state as the ground state in zero field. We here investigate the ground state of the same model under an in-plane magnetic field. The spin Hamiltonian is given by

$$\mathcal{H} = \sum_n \sum_i J_n \mathbf{S}_i \cdot \mathbf{S}_{i+n} + \sum_i [K_{1212} (\mathbf{S}_i \cdot \mathbf{S}_{i+1})^2 + K_{1223} (\mathbf{S}_i \cdot \mathbf{S}_{i+1})(\mathbf{S}_{i+1} \cdot \mathbf{S}_{i+2})] - h \sum_i S_i^x. \quad (\text{S1})$$

Here, we introduce the RKKY interaction  $J_n = -J_1[\cos(k_1 n)/k_1 n] - J_2[\cos(k_2 n)/k_2 n]$  up to the 10th nearest neighbor ( $n = 10$ ), where we set  $J_1 = 1$  as the energy unit, and  $k_1 = 0.29\pi$  and  $k_2 = \pi$  in line with our RXS data. The second and third terms in Eq. (S1) are the four-spin exchanges with  $K_{1212}, K_{1223} > 0$ , which arise from perturbative expansions of the spin-charge coupling in the Kondo lattice model. The last term in Eq. (S1) represents the Zeeman coupling to an in-plane magnetic field  $h \parallel x$ . We assume  $XY$  spins with  $|\mathbf{S}_i| = 1$ .

We performed simulated annealing with  $N = 200$  spins for several parameter sets on Eq. (S1). In this process, the parameter  $J_2$  was tuned according to the structure of the exchange interactions in momentum space,  $J_{\mathbf{Q}}$ . Figures S5(a) and S5(b) show zero-field ground-state phase diagrams as a function of  $K_{1212}$  and  $K_{1223}$  for  $J_2 = 1$  and  $J_2 = 2.0667$ , respectively. The  $\mathbf{Q}_1$  modulation dominates in the former [Fig. S5(a)], where the ratio of  $J_{\mathbf{Q}}$  is  $J_{\mathbf{Q}_2}/J_{\mathbf{Q}_1} = 0.2$ . In this case, the introduction of finite  $K_{1223}$  value is necessary to stabilize a double- $\mathbf{Q}$  broken-helix state, as mentioned in Ref. [9]. Conversely, the  $\mathbf{Q}_2$  modulation is dominant in the latter [Fig. S5(b)], where  $J_{\mathbf{Q}_2}/J_{\mathbf{Q}_1} = 1.3$ . In this case, a double- $\mathbf{Q}$  broken-helix state can be stabilized without introducing the  $K_{1223}$  term.

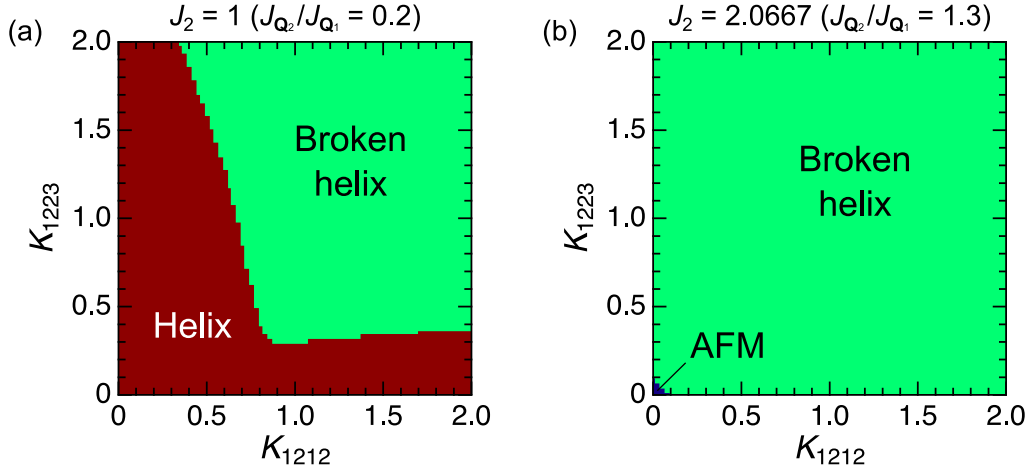


FIG. S5. Ground-state phase diagram of Eq. (S1) as a function of  $K_{1212}$  and  $K_{1223}$  in zero field for (a)  $J_2 = 1$  ( $J_{\mathbf{Q}_2}/J_{\mathbf{Q}_1} = 0.2$ ) and (b)  $J_2 = 2.0667$  ( $J_{\mathbf{Q}_2}/J_{\mathbf{Q}_1} = 1.3$ ). “Helix” represents a single- $\mathbf{Q}$  helix state, which appears in a wide parameter ranges of  $K_{1212}$  and  $K_{1223}$  for  $J_2 = 1$ .

Figure S6 shows the magnetic-field dependence of magnetization  $m$  and spin structure factor, defined as  $S(\mathbf{q}) = (1/N) \sum_{i,j} \langle \mathbf{S}_i \cdot \mathbf{S}_j \rangle e^{i\mathbf{q} \cdot (\mathbf{r}_i - \mathbf{r}_j)}$ , at various  $\mathbf{Q}$  positions for  $J_2 = 2.0667, K_{1212} = 0.2, K_{1223} = 0$  [(a)–(c)] and for  $J_2 = 2.0667, K_{1212} = 0.4, K_{1223} = 0$  [(d)–(f)]. We note that the moderate introduction of the  $K_{1223}$  term does not significantly alter the results. At  $h = 0$ ,  $S(\mathbf{Q}_1)/S(\mathbf{Q}_2) \approx 0.13$  and  $0.22$  for  $K_{1212} = 0.2$  and  $0.4$ , respectively. These values closely match our experimental observation of  $I_{\mathbf{Q}_1}/I_{\mathbf{Q}_2} \approx 0.17$  for sample #1 ( $q_{1z} = 0.29$ ). However, the  $\mathbf{Q}_1$  component suddenly disappears in a high-field phase above a metamagnetic transition. Furthermore, there is no discernible tendency for the enhancement of higher-harmonic modulations. These results are in qualitative contradiction with our experimental observation of a double- $\mathbf{Q}$  broken-fanlike state, as shown in Figs. 3 and 4 in the main text. We hence conclude that the magnetism in  $\text{EuIn}_2\text{As}_2$  cannot be perfectly reproduced by the spin Hamiltonian Eq. (S1). This would be because the incorporation of the Heisenberg exchange interactions only along the 1D chain is insufficient to adequately describe the RKKY interaction in real 3D systems. As an alternative, we propose in the main text that an effective spin Hamiltonian composed of exchange interactions in momentum space is useful for describing the helimagnetism characterized by interplane magnetic modulations with intraplane ferromagnetic couplings.

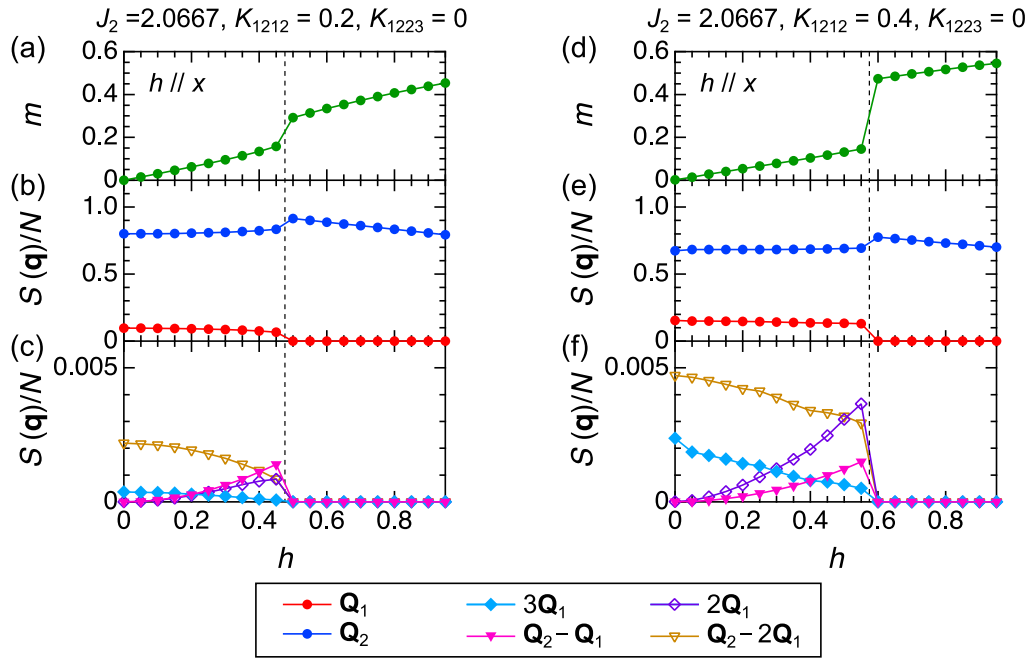


FIG. S6. Magnetic-field dependence of magnetization  $m$  (top) and spin structure factor  $S(\mathbf{q})$  per a spin at several  $\mathbf{Q}$  positions (bottom) for  $h \parallel x$ , calculated by simulated annealing for Eq. (S1) with  $J_2 = 2.0667$ ,  $K_{1212} = 0.2$ ,  $K_{1223} = 0$  [(a)–(c)] and  $J_2 = 2.0667$ ,  $K_{1212} = 0.4$ ,  $K_{1223} = 0$  [(d)–(f)].

- 
- [1] F. Izumi and K. Momma, Three-Dimensional Visualization in Powder Diffraction, *Solid State Phenom.* **130**, 15 (2007).
- [2] A. M. Goforth, P. Klavins, J. C. Fettinger, and S. M. Kauzlarich, Magnetic Properties and Negative Colossal Magnetoresistance of the Rare Earth Zintl phase  $\text{EuIn}_2\text{As}_2$ , *Inorg. Chem.* **47**, 11048 (2008).
- [3] Y. Zhang, K. Deng, X. Zhang, M. Wang, Y. Wang, C. Liu, J.-W. Mei, S. Kumar, E. F. Schwier, K. Shimada, C. Chen, and B. Shen, In-plane antiferromagnetic moments and magnetic polaron in the axion topological insulator candidate  $\text{EuIn}_2\text{As}_2$ , *Phys. Rev. B* **101**, 205126 (2020).
- [4] F. H. Yu, H. M. Mu, W. Z. Zhuo, Z. Y. Wang, Z. F. Wang, J. J. Ying, and X. H. Chen, Elevating the magnetic exchange coupling in the compressed antiferromagnetic axion insulator candidate  $\text{EuIn}_2\text{As}_2$ , *Phys. Rev. B* **102**, 180404(R) (2020).
- [5] J.-R. Soh, A. Bombardi, F. Mila, M. C. Rahn, D. Prabhakaran, S. Francoual, H. M. Rønnow, and A. T. Boothroyd, Understanding unconventional magnetic order in a candidate axion insulator by resonant elastic x-ray scattering, *Nat. Commun.* **14**, 3387 (2023).
- [6] S. X. M. Riberolles, T. V. Trevisan, B. Kuthanazhi, T. W. Heitmann, F. Ye, D. C. Johnston, S. L. Bud'ko, D. H. Ryan, P. C. Canfield, A. Kreyssig, A. Vishwanath, R. J. McQueeney, L.-L. Wang, P. P. Orth, and B. G. Ueland, Magnetic crystalline-symmetry-protected axion electrodynamics and field-tunable unpinned Dirac cones in  $\text{EuIn}_2\text{As}_2$ , *Nat. Commun.* **12**, 999 (2021).
- [7] CrysAlisPro (Agilent Technologies Ltd, Yarnton, 2014).
- [8] V. Petříček, M. Dušek, and L. Palatinus, Crystallographic computing system JANA2006: General features, *Z. Kristallogr. Cryst. Mater.* **229**, 345 (2014).
- [9] E. Donoway, T. V. Trevisan, A. Liebman - Peláez, R. P. Day, K. Yamakawa, Y. Sun, J. R. Soh, D. Prabhakaran, A. Boothroyd, R. M. Fernandes, J. G. Analytis, J. E. Moore, J. Orenstein, and V. Sunko, Symmetry-breaking pathway towards the unpinned broken helix, arXiv:2310.16018.